*IEEE Open Journal of*
**Antennas and Propagation**

# A Step-by-Step Design Methodology for Broadband Tunable Microwave Metasurface Absorbers Using Theory of Characteristic Modes

**Zihao Ning**[*], **Mengmeng Li**[*], *Senior Member, IEEE*, **Dazhi Ding**[*], *Senior Member, IEEE*, **Xia Ai**[†], **Jiaqi Liu**[†], and **Chao-Fu Wang**[‡], *Senior Member, IEEE*

[1]School of Microelectronics (School of Integrated Circuits), Nanjing University of Science and Technology, Nanjing, China
[2]National Key Laboratory of Science and Technology on Test Physics and Numerical Mathematics, Beijing, China
[3]Department of Electrical and Computer Engineering, National University of Singapore, Singapore

CORRESPONDING AUTHOR: Mengmeng Li (e-mail: limengmeng@njust.edu.cn).

**ABSTRACT** In this paper, a characteristic mode (CM)-based design methodology is developed for the reconfigurable microwave metasurface absorbers (MMA) with using commercially available substrates. Theoretical intrinsic connection between modal behaviors and absorption properties is first formulated for the design of the structures. As a proof of the method, a broadband MMA consisting of butterfly elements is step-by-step designed. The positions and values of the impedance loading are determined based on the modal significances and modal currents for broadband operation. The absorption performance is evaluated by the formulated theoretical model and verified by full-wave simulation. After that, a flexible implementation a employed for free-form surfaces conformal. Experimentally, the proposed MMA is fabricated and measured. The absorption fractional bandwidth with reflectivity less than -10 dB is achieved from 3.6 to 11.6 GHz (105%). Good agreements between the simulation and measurement results for both planar and cylindrical cases validate the developed CM-based design methodology. The mimicry of time-varying scattering cross section (SCS) is then further realized through real-time coding absorption states, which is a promising candidate for practical electromagnetic systems.

**INDEX TERMS** Theory of characteristic modes, metasurface absorber, reconfigurable, flexible, scattering cross section.

## I. INTRODUCTION

THE design of microwave absorber [1]- [9] is of great significance in many applications. Conventional absorbing materials, such as carbon and ferrite [2], [3], cannot be well integrated with electromagnetic (EM) structures due to their large volume and high density. The Salisbury screen with an impedance matching layer separated from the ground by a quarter wavelength is proposed to realize the perfect absorption through phase cancellation. Despite their simple structure and lightweight, the bandwidth of absorption is usually very narrow [4]. The Jauman absorber with a multilayer structure extends the absorption bandwidth while increasing the thickness of its structure [5].

The metasurface [10], as a 2-D periodic array, has been widely applied to achieve EM absorption and scattering cross section (SCS) reduction in terms of phase [11], [12], amplitude [13]- [16], and polarization [17] due to their strong potential and effective manipulation of electromagnetic waves. Conventional metasurfaces are typically passive structures that lack post-processing operational flexibility. To mitigate this problem, tunable/reconfigurable metasurfaces for variable absorption have drawn great interest in recent years [18]- [33]. The flow of liquid crystal molecules has been employed to switch the absorption and transmission states of visible light [19], [20], respectively. The reconfigurable surface impedance has been obtained by changing the

bias voltage of graphene to realize the modulations of amplitude [21]- [23]. Furthermore, the modulations of the phase, amplitude, and frequency of EM wave can be achieved by loading the lumped elements, such as varactor diodes [26]- [28], positive-intrinsic-negative (PIN) diodes [29]- [33] onto the designed metasurfaces. Despite the significant application potential of the reconfigurable metasurfaces, there are usually limited to planar structures that cannot fit well for free-form surface.

With promising applications in the field of electromagnetic absorption, the development of metasurface absorbers-oriented design methods is receiving increasing attention. Over the last decade, equivalent circuit modeling (ECM) has gained significant momentum regarding its simple and analytical expressions. However, it faces great difficulties in describing complex structures due to the lack of field analysis, which loses its appealing features of simplicity and effectiveness. For this reason, recent studies have indicated that the theory of characteristic mode (TCM) [34], [35] is an effective method to guide the design of metasurfaces from a physical perspective [16], [36]- [39]. In [37], the modal behaviors with different loaded resistances have been analyzed for active frequency selective surface using the TCM to obtain reconfigurable transmission/reflection. It is found that the isolation between transmission and reflection states is mainly determined by the radiation field from fundamental mode. In [38], the elements with a phase range of $2\pi$ and a transmission coefficient higher than 0.8 has been realized by exciting the two characteristic modes with a certain phase difference. It also has been applied for the design of frequency-selective rasorber where the absorption has been achieved by placing resistors based on the analysis of modal significances and modal currents [39]. However, most of the TCM-based works presented in literatures so far lack a theoretical model being able to clearly guide enhance the design process of reconfigurable microwave metasurface absorbers (MMA), and the development of such kind of TCM-based design methodology would have good prospects for designing high-performance reconfigurable MMAs to meet application requirements.

The main objective of this paper focuses on how to use commercially available substrates to create pattern elements with discrete loadings, such as diodes, to effectively design high-performance tunable MMAs. These substrates could be assumed lossless as their loss tangents are usually very low at the designed frequency. Such kind of low loss of the substrates will not change their CM behavior much as demonstrated in the CM design of microstrip antennas and consequently low substrate loss does not contribute to absorption directly much as compared to the good design of absorption structures to achieve better impedance matching with the free space. By showing the theoretical intrinsic connection between modal behaviors and absorption properties, we will develop a design methodology for applying the TCM to guide the design of MMAs with using commercially

available substrates. Based on this, a broadband tunable MMA is presented, the absorption properties of which are realized through properly loading PIN diodes onto each element guided by its modal behaviors. Fabricated flexible prototypes are measured on planar and cylindrical foams to validate their absorption performances. The results show that less than -10 dB reflection over a broadband range from 3.6 to 11.6 GHz (105%) with multistate switchable is achieved for both planar and cylindrical cases. All in all, the contributions of this work are summarized as follows.

1) The TCM-based design methodology for broadband metasurface absorbers with using commercially available substrates is developed, where a mathematical model that map the theoretical intrinsic connection between modal behaviors and absorption properties is first established to theoretical analyze and directly guide the design of the structure.

2) The step-by-step design process is summarized by selecting a butterfly-shape structure to provide a detailed and comprehensive illustration of the implementation of broadband metasurface absorber design using TCM.

3) Incorporated with flexible and programming, the designed MMAs can achieve broadband absorption (105%) on free-form surfaces with high-precision modulation, helping to experimentally explore the potential of metasurface for electromagnetic mimicry applications.

This paper is organized as follows. In Section II, the CM design methodology for MMAs with using commercially available substrates is presented. In Section III, the CM-based design process for the MMA is introduced and summarized. After that, we improve the element to a flexible structure that can be applied to free-form surfaces. Fabrication and measurement results of the flexible prototypes are presented to verify the absorption performances in Section IV. Finally, concluding remarks are given in Section V.

## II. DESIGN METHODOLOGY

### A. Problem Description

In general, a typical MMA consists of a patterned structure printed on the grounded dielectric substrate and can be modeled with two-port network, as shown in Fig. 1. When an EM wave impinges the MMA, the EM energy can only be reflected or absorbed due to the presence of the metallic screen that forbids EM field transmission. We can thus define the absorption rate (AR) as $\mathrm{AR}(\omega) = 1 - |S_{11}|^2$, used to describe the operating performance. Ideally, the S-parameter of MMA should meet the conditions, $|S_{11}| = 0$ in the band of interest. In other words, the input impedance $Z_{\mathrm{in}}$ of the two-port network should be close to the free-space impedance $Z_{\mathrm{air}}$ (377 Ohm) [22]. This can be achieved by adjusting the equivalent impedance $Z_{\mathrm{top}}$ of the top layer patterned structure. For passive structures, adjusting their geometrical parameters is a widespread method, but the operating bandwidth is usually limited. This can be effectively addressed by suitable loading resistors, but the EM response cannot
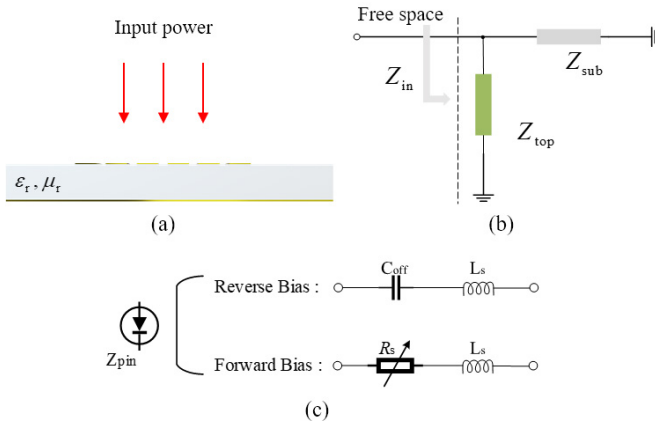
**FIGURE 1.** Microwave metesurface absorber. (a) General profile sketch, (b) two-port representation and (c) ECM of the PIN diode.

be altered once they have been manufactured. PIN diodes, because of variable resistance features under forwarding bias currents, are often used to adjust the $Z_{in}$ to achieve tunable absorption [29]- [31]. Usually, the impedance $Z_{pin}$ represents the equivalent resistor-inductor-capacitor (RLC) circuit parameters of the PIN diode and can be modeled in two scenarios: (i) capacitance $C_{off}$ for reverse bias voltage, and (ii) variable resistance $R_s$ for forwarding bias current as shown in Fig. 1(c).

The reflection coefficient $S_{11}$ of the MMA can be easily obtained after the circuit topology and component values are determined. Extensive works [14], [29], [32] have demonstrated that equivalent circuit model (ECM) can be used to reliably analyze the operating mechanisms and performance of a structure. However, it lacks the explicit EM field insight to effectively guide the design process of MMA from a selective patterned structure to final impedance-matched structure. Especially for complex structures, accurate ECM modelling presents great difficulties and also loses its appeal of simplicity and efficiency. Therefore, by revealing the theoretical intrinsic connection between the changes of $S_{11}$ and modal behaviors, the TCM is introduced in this paper to develop a design methodology for tunable MMAs that guides the design from a physical and intuitive perspective. It is expected that the developed design methodolgy will also be complementary to the ECM-based one.

### B. TCM-Based Theoretical Model

CM analysis can help decompose the scattering of structure into a superposition of different orthogonal modes [34]. For a grounded metasurface, considered as a layered media structure with infinite lateral dimension, the grounded dielectric substrate produces a reflected field $\mathbf{E}^r$ under the action of the incident field $\mathbf{E}^i$. The conducting surface of the metasurface will generate an induced current $\mathbf{J}$ and excite a scattered field $\mathbf{E}^s$ at the same time. According to the boundary condition on the conducting surface, the total electric fields should satisfy

the equation as follow

$$\mathbf{n} \times \mathbf{E}^s = -\mathbf{n} \times (\mathbf{E}^i + \mathbf{E}^r) = -\mathbf{n} \times (\mathbf{E}^{ex}) \qquad (1)$$

where $\mathbf{n}$ is the unit outward normal vector of the conducting surface. As the scattered field $\mathbf{E}^s$ can be expressed as the sum of the vector $\mathbf{A}$ and scalar $\Phi$, the mixed potential integral equation (MPIE) for (1) can be written as [40], [41]

$$j\omega\mu_0 \mathbf{n} \times \left[ \mathbf{A}(\mathbf{r}) + \frac{1}{k_0^2}\nabla\Phi(\mathbf{r}) \right] = \mathbf{n} \times (\mathbf{E}^{ex}) \qquad (2)$$

where

$$\mathbf{A}(\mathbf{r}) = \iint_S \bar{\mathbf{G}}_A(\mathbf{r}, \mathbf{r}') \cdot \mathbf{J}(\mathbf{r}')ds' \qquad (3)$$

$$\Phi(\mathbf{r}) = \iint_S G_q(\mathbf{r}, \mathbf{r}')\nabla \cdot \mathbf{J}(\mathbf{r}')ds' \qquad (4)$$

in which $\mathbf{J}$ is the unknown current on the metasurface, $\bar{\mathbf{G}}_A$ denotes the Greens function for the magnetic vector potential, and $G_q$ denotes the Greens function for the electric scalar potential.

From the standard MPIE of a layered media structure, a method of moments (MOM) impedance matrix $\mathbf{Z} = \mathbf{R} + j\mathbf{X}$ can be obtained, where $\mathbf{R}$ is the real Hermitian part of $\mathbf{Z}$, and $\mathbf{X}$ is the imaginary Hermitian part of $\mathbf{Z}$. The CMs of the structure are then defined through the following generalized eigenvalue equation $\mathbf{X}\mathbf{J}_n = \lambda_n \mathbf{R}\mathbf{J}_n$, so that the total current $\mathbf{J}$ on the conducting surface can be decomposed as $\mathbf{J} = \sum_{i=1}^{N} \alpha_i \mathbf{J}_i$ with N modal currents $\mathbf{J}_n$ [34], [35]. The magnitude of modal weighting coefficient (MWC) $\alpha_n$ measures the contribution of each $\mathbf{J}_n$ to the total current $\mathbf{J}$. A more convenient way of estimating the proportion is by defining the factor of $\alpha_n$ as the modal significance ($MS_n = 1/|1 + j\lambda_n|$). In general, CMs with MS greater than $1/\sqrt{2}$ (0.707) are significant modes.

Once the surface characteristic currents $\mathbf{J}_n$ are obtained, the scattered power $p^s$ by $\mathbf{J}$ can also be expanded in the following form

$$p^s = -\iiint_V \mathbf{J}^* \cdot \mathbf{E}^s dV = \iiint_V \mathbf{J}^* \cdot \mathbf{Z}\mathbf{J}dV$$

$$= \iiint_V (\sum_{i=1}^{N} \alpha_i \mathbf{J}_i)^* \cdot \mathbf{Z}(\sum_{j=1}^{N} \alpha_j \mathbf{J}_j)dV$$

$$= \iiint_V (\sum_{i=1}^{N} |\alpha_i|^2 \mathbf{J}_i^* \cdot \mathbf{Z}\mathbf{J}_i + \sum_{j\neq i}^{N}\sum_{i=1}^{N} \alpha_i^* \alpha_j \mathbf{J}_i^* \cdot \mathbf{Z}\mathbf{J}_j)dV$$

$$= \sum_{i=1}^{N} |\alpha_i|^2 \iiint_V \mathbf{J}_i^* \cdot \mathbf{Z}\mathbf{J}_i dV + \sum_{j\neq i}^{N}\sum_{i=1}^{N} \alpha_i^* \alpha_j \iiint_V \mathbf{J}_i^* \cdot \mathbf{Z}\mathbf{J}_j dV$$

$$\qquad (5)$$

Here the characteristic current $\mathbf{J}_n$ are normalized using the operator $R$, the former term indicates the total scattered power of mode $i$, and the latter term indicates the coupling power of mode $i$ to mode $j$. For the closed surface $S_\infty$ at infinity (far-field), the scattered electric fields of the different

CMs are orthogonal to each other and the above equation can be written as

$$
\begin{aligned}
p^{\mathrm{s}} &= \sum_{i=1}^{N} |\alpha_i|^2 \cdot (1+j\lambda_i)\, \delta_{ii} + \sum_{j \neq i}^{N} \sum_{i=1}^{N} \alpha_i^* \alpha_j \cdot (1+j\lambda_j)\, \delta_{ij} \\
&= \sum_{i=1}^{N} |\alpha_i|^2 \cdot (1+j\lambda_i)
\end{aligned}
\tag{6}
$$

According to MPIE, the real part of $p^{\mathrm{s}}$ denote the contribution $p^{\mathrm{sc}}$, namely captured power $p^{\mathrm{c}}$, by conducting surface, while the imaginary part of $p^{\mathrm{s}}$ can be considered as the contribution $p^{\mathrm{sg}}$ by infinite grounded dielectric substrate [34].

For the grounded metasurface with impedance loading $Z_{\mathrm{pin}} = R_{\mathrm{s}} + jX_{\mathrm{s}}$, the standard MPIE is rewritten as $(Z + Z_{\mathrm{pin}})\mathbf{J} = \mathbf{E}^{\mathrm{ex}}$ to illustrate the role of $Z_{\mathrm{pin}}$ on the eigen solutions and give the following CM formulation [42]

$$
(\mathbf{X} + \mathbf{X}_{\mathrm{s}})\mathbf{J}_n = \lambda_n (\mathbf{R} + \mathbf{R}_{\mathrm{s}})\, \mathbf{J}_n \tag{7}
$$

The eigenvalues have the following physical interpretation

$$
\lambda_n = \frac{p_n^{\mathrm{sg}}}{p_n^{\mathrm{c}}} = \frac{p_n^{\mathrm{sg}}}{p_n^{\mathrm{sc}} + p_n^{\mathrm{d}}} \tag{8}
$$

where the power quantities can be expressed as

$$
\begin{aligned}
p_n^{\mathrm{sc}} &= \frac{1}{2} \int_V \mathrm{Re}(Z)\|J_n\|^2 dV = \langle \mathbf{J}_n^*, \mathbf{R}\mathbf{J}_n \rangle \\
p_n^{\mathrm{d}} &= \frac{1}{2} \int_V \mathrm{Re}(Z_{\mathrm{pin}})\|J_n\|^2 dV = \langle \mathbf{J}_n^*, \mathbf{R}_{\mathrm{s}}\mathbf{J}_n \rangle \\
p_n^{\mathrm{sg}} &= \frac{1}{2} \int_V \mathrm{Im}(Z + Z_{\mathrm{pin}})\|J_n\|^2 dV = \langle \mathbf{J}_n^*, (\mathbf{X} + \mathbf{X}_{\mathrm{s}})\mathbf{J}_n \rangle
\end{aligned}
\tag{9}
$$

As described above, since the PIN diode is loaded on the conducting surface, the optimum absorption $\mathrm{AR}(\omega)$ achieved is by converting almost all of the captured power $p^{\mathrm{c}}$ of conducting surface into thermal power $p^{\mathrm{d}}$, that is $p^{\mathrm{d}} \gg p^{\mathrm{sc}}$. The expression for the reflection coefficient $S_{11}$ can be approximated as

$$
\begin{aligned}
|S_{11}|^2 &= 1 - \mathrm{AR}(\omega) = 1 - \left| \frac{p^{\mathrm{d}}}{p^i} \right| \\
&= 1 - \frac{\sum e_n^{\mathrm{d}} |\alpha_n|^2}{|\langle \mathbf{E}^{\mathrm{ex}}, \mathbf{J}^* \rangle|} \approx 1 - \frac{\displaystyle\sum_{n=1}^{N} |\alpha_n|^2}{\left| \displaystyle\sum_{n=1}^{N} |\alpha_n|^2 \cdot (1+j\lambda_n) \right|}
\end{aligned}
\tag{10}
$$

where the thermal conversion rate $e_n^{\mathrm{d}} = |p_n^{\mathrm{d}}/p_n^{\mathrm{c}}| \approx 1$ denotes almost all of the captured power $p^{\mathrm{c}}$ into thermal power $p^{\mathrm{d}}$ and the external input power $p^i = \langle \mathbf{E}^{\mathrm{ex}}, \mathbf{J}^* \rangle = -(p^{\mathrm{sc}} + p^{\mathrm{d}} + p^{\mathrm{sg}})$ for the case of a half-space constructed with infinitely grounded dielectric substrate. It can be seen that there are two aspects that should be addressed in order to optimize the absorption performance: (i) improve the MS of the CMs and achieve good impedance matching with $Z_{\mathrm{air}}$ by loading impendence, and (ii) improve the thermal conversion rate

$e_n^{\mathrm{d}}$ through loading impedance in the area of concentrated current distribution.

### C. Design Guidelines
Based on the above analysis, the following guidelines are applied to design a MMA with impedance loading for broadband tunable absorption.

Step 1) Patterned structure selection and ECM. According to the analysis of equivalent circuit, in one element of MMA, the PIN diode as an impedance loading device can be used to adjust $Z_{\mathrm{in}}$ to achieve absorption conditions, $|S_{11}| = 0$. Therefore, when selecting the pattern structure, it should be considered to facilitate the simultaneous satisfaction of impedance matching and feeding design.

Step 2) Modal behaviors analysis. For a given patterned structure, calculating its modal behaviors and plot the corresponding modal far-field patterns and modal currents. Based on the modal behaviors, find the dominant mode that contributes most to the scattered electric field $\mathbf{E}^{\mathrm{s}}$, namely operating mode. Optimization of the structural parameters so that the operating mode lies within the band of interest.

Step 3) Efficient optimization for broadband operation. Implementation of the CM analyses of the patterned structure with impedance loading clearly shows that the captured energy $p^{\mathrm{c}}$ can be efficiently converted into thermal power $p^{\mathrm{d}}$ only if the impedance $Z_{\mathrm{pin}}$ is loaded in the area of concentrated current distribution. The absorption properties can be evaluated using Eq. (10) and optimized by the impedance to directly result in the broadband operation.

Step 4) Full-wave validation and finalization. With the estimated results, the full-wave simulator CST can be used to optimize and finalize the MMA.

Some benefits of the proposed design methodology can be seen from the above guidelines. First, PIN diodes as resistor-adjustable devices can provide more design freedom. Thanks to the fact that the MOM is good at dealing with irregular structures, the proposed methodology is not affected by the complexity of the patterned structure. Moreover, observed physical insight into the scattering mechanism of the patterned structure can be extracted as an important guideline for improving its EM wave manipulations and design. Therefore, the above guidelines can provide a generalized directional fast optimization procedure used to broadband tunable absorption design for a given patterned structure.

## III. DESIGN OF THE MMA
### A. Patterned Structure Selection and ECM
Considering that the degenerate modes of a symmetric structure are reciprocal, without loss of generality, a metasurface consisting of butterfly-shaped structures is employed here to illustrate the implementation process of the proposed step-by-step design methodology. The proposed geometrical structure of the element is shown in Fig. 2. The butterfly-shaped structure is designed on the grounded substrate with
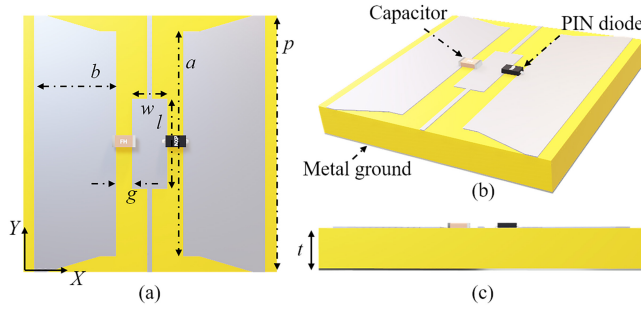
This article has been accepted for publication in IEEE Open Journal of Antennas and Propagation. This is the author's version which has not been fully edited and content may change prior to final publication. Citation information: DOI 10.1109/OJAP.2023.3336610

IEEE Open Journal of
Antennas and Propagation



**FIGURE 2.** Geometrical structure of the element, (a) top, (b) perspective, and (c) side view.

a relative permittivity of 3. The PIN diode, as a resistive adjustable device, is placed at the gap between the trapezoidal patch and the central microstrip line of the butterfly-shaped patch to achieve the variable absorption states. When a number of elements are distributed periodically into a planar array, all the elements of each column are interconnected with each other in the longitudinal direction. The bias current can be conducted through the trapezoidal patches and grounded by the central microstrip to generate a forward bias current on the PIN diodes.

The ECM for the element is shown in Fig. 3. For the $x$-polarization incident plane wave, as shown in Fig 3(a), the inductance $L_1$, $L_2$, $L_3$ are produced due to the induced currents on the top metallic layer and they can be expressed in terms of a total inductance $L_e$. Similarly, the capacitance $C_1$, $C_2$, and $C_d$ are produced due to the voltage difference between adjacent metal parts. According to the transmission line theory, the input impedance $Z_{in}$ of the element can be expressed as

$$Z_{in} = Z_{top} \parallel jZ_{sub} \tan(\beta t)$$
$$= \left[ j\omega L_e \parallel \left( \frac{1}{j\omega C_1} + \frac{1}{j\omega C_2} \right) + \frac{1}{j\omega C_d} \right] \parallel jZ_{sub} \tan(\beta t)$$
(11)

where $Z_{sub}$, $d$, and $\beta$ are the intrinsic impedance, thickness, and propagation constant of the substrate, respectively.

As a comparison, the ECM of the final element with PIN diode is also given in Fig. 3(b), and its input impedance $Z_{in}$ can be written as

$$Z_{in} = Z_{top} \parallel jZ_{sub} \tan(\beta t)$$
$$= \left[ \left( Z_{pin} + \frac{1}{j\omega C_v} + j\omega L_e \right) \parallel \left( \frac{1}{j\omega C_1} + \frac{1}{j\omega C_2} \right) + \frac{1}{j\omega C_d} \right]$$
$$\parallel jZ_{sub} \tan(\beta t)$$
(12)

in which $C_v$ represent the equivalent RLC circuit parameters of the loaded capacitor. In general, these equivalent circuits are difficult to model quickly and accurately numerically by parameter extraction, especially for the butterfly-shaped structure shown in Fig. 2. The design process of the elements from (14) to (15) is next detailed through CM analysis.
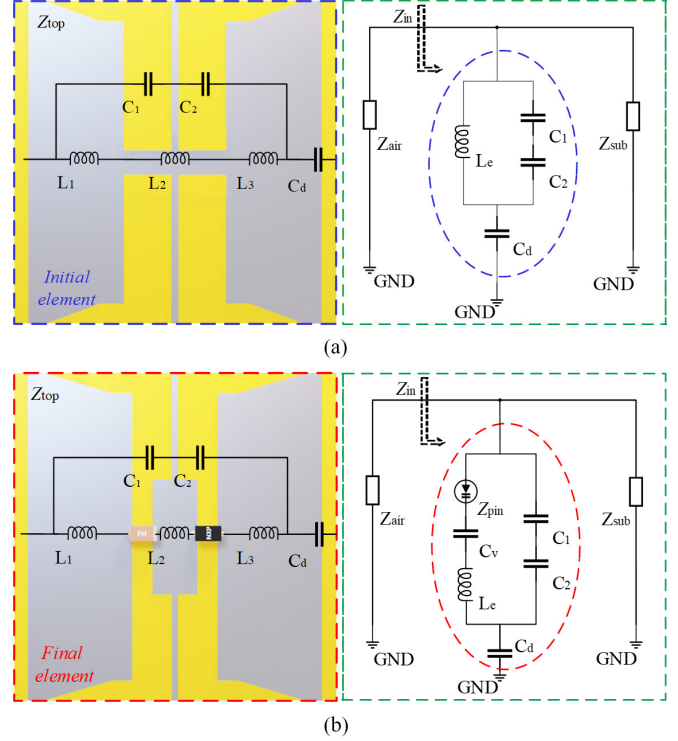


**FIGURE 3.** Equivalent circuit model of (a) the initial element and (b) the final element.

### B. Modal Behavior Analysis

For simplicity, the grounded dielectric substrate is assumed to be lossless and of infinite dimension. Firstly, we study the modal behaviors of the butterfly-shaped structure. The MS of the first four modes are shown in Fig. 4(a). It can be observed that modes 1 to 3 are significant in the frequency band of 4 to 12 GHz, and the other modes can be ignored due to the small value of their MSs. Fig. 4(b) depicts the modal field (far-field) patterns and modal currents of modes 1-3 at the frequencies of 6.0 GHz, 10 GHz, and 11.4 GHz, respectively. For the modal far-field pattern, modes 1 and 2 have broadside radiation patterns while mode 3 has a split radiation lobe. This suggests that mode 3 makes a smaller contribution to the scattered power in the normal direction. For the modal currents, $\mathbf{J}_1$ of mode 1 mainly concentrates in the area within the solid line of Fig. 4(b), $\mathbf{J}_2$ of mode 2 mainly distributes along the area within the dashed line of Fig. 4(b), and the modal current $\mathbf{J}_3$ mainly distributes along the area inside the chain line of Fig. 4(b). Therefore, to decrease the scattered fields of the structure, the position with concentrated energy of mode 1 is the most suitable choice to place the PIN diode.

The parametric study is carried out to understand the effect of different dimensions on MS. Only one parameter is changed during the parametric study. Fig. 5 shows the MSs when $a$ and $g$ are tuned. As shown in Fig. 5(a), when $a$ decreases, the resonant frequency of mode 3 shifts upward, and the resonant frequencies of modes 1 and 2 remain
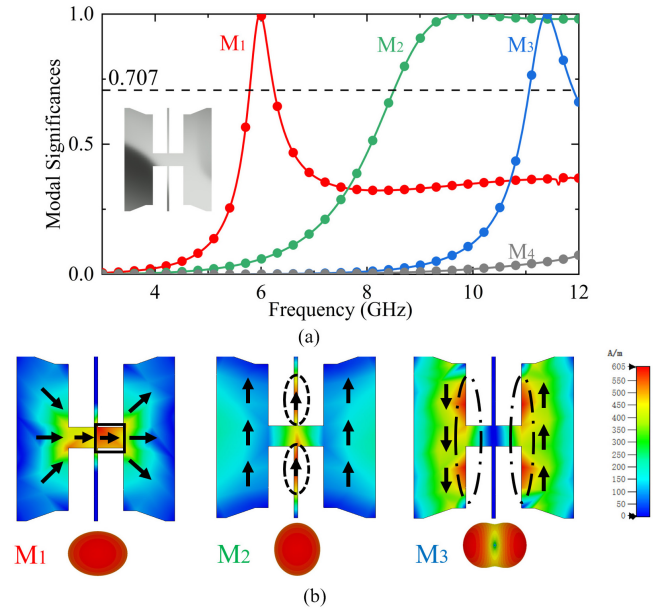
**FIGURE 4.** CM analysis for the butterfly-shaped structure. (a) MSs, (b) the corresponding mode current distribution and far-field pattern. ($p = 8$ mm, $a = 7$ mm, $b = 2$ mm, $g = 1$ mm, $t = 4$ mm)
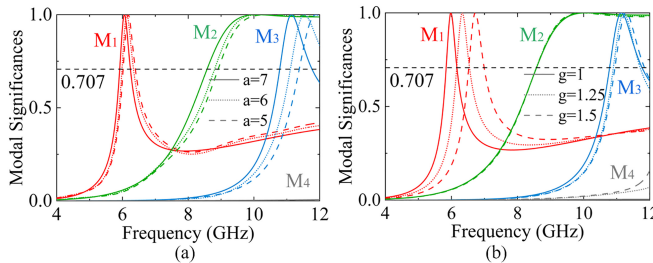


**FIGURE 5.** Effects of different (a) $a$ and (b) $g$ on MS of the butterfly-shaped structure.

essentially unchanged. This can be explained by the fact that the $\mathbf{J}_3$ mainly distributes along the area inside the blue dashed and a decrease of $a$ significantly affects the path length of $\mathbf{J}_3$, leading to an upward shift of the resonant frequency. Similarly, Fig. 5(b) shows that the dimension of $g$ mainly determines the path length of $\mathbf{J}_1$, with the resonant frequency of mode 1 decreasing as $g$ increases, while modes 2 and 3 are almost unaffected. The other parameters have a similar effect and are not shown here for the sake of brevity. It should be noted that the structural parameters given in Fig. 4 are optimized making mode 1 lies within the band of interest.

### C. Efficient Optimization for Broadband Operation
Then, we use the CM analysis again to analyze the butterfly-shaped structure with PIN diode. The diagonal matrix $\mathbf{Z}_{\text{pin}}$, describe the loaded impedance, is added in MoM impedance matrix $\mathbf{Z}$ to represent modelling the ECM in the MoM [43]. The NXP BAP70-03 PIN diode [44] is chosen here to regulate the input impedance $Z_{\text{in}}$. In the OFF state, it is equivalent to a 0.57 pF capacitance in series with a 1
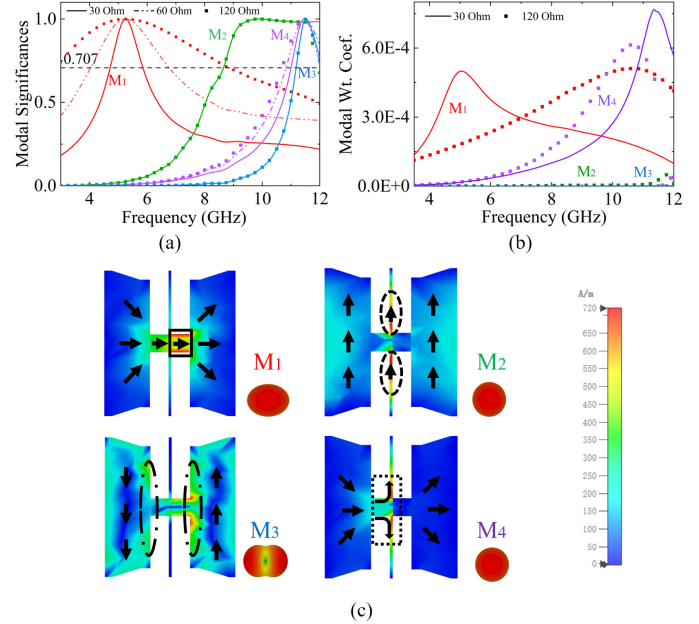


**FIGURE 6.** CM analysis for the butterfly-shaped structure with PIN diode. (a) MSs and (b) MWCs with different $R_{\text{s}}$, and (c) the corresponding modal currents distribution and far-field patterns.

nH parasitic inductance, while in the ON state, it can be seen as a variable resistance $R_{\text{s}}$ in series with the same parasitic inductance. Fig. 6(a) depicts the MS of the first four modes, it can be seen that the bandwidth of mode 1 increases gradually with increasing $R_{\text{s}}$, but the bandwidth of the other modes remain constant due to the small amplitude of the modal currents at the PIN diode loading position. Note that the loading of the PIN diode causes mode 4 to become significant in the band of interest, shown in Fig. 6(a) and (b). The corresponding modal far-field patterns and modal currents are given in Fig. 6(c). Compared to the results of the CM analysis without PIN diode, the modal far-field patterns and modal currents of modes 1 to 3 remain constant. However, the presence of multiple modes (mode 1 and mode 4) would deteriorate the absorption performance of the structure as mode 4 has a broadside radiation field similar to that of mode 1 and the energy is not converted into thermal power.

Using Eq. (10) we can evaluate the absorption properties, but it should be noted that the modal far-fields of the two significant modes have to satisfy orthogonality. Therefore, in Fig. 7, we show the modal far-field orthogonality of modes i and j up to order 4 at 10 GHz. Considering modal far-field as frequency-independent basis patterns, the modal far-field orthogonality at 10 GHz can be used for broadband calculations [45]. The modal far-fields are perfectly orthogonal to each other for PEC, and for the structure with $R_{\text{s}}$=30 Ohm, the modal far-field nonorthogonality of the two significant modes (mode1 and mode4) can be neglected. The reflection coefficients $S_{11}$ evaluated with different numbers of CMs, respectively, are given in Fig. 8. The results show that
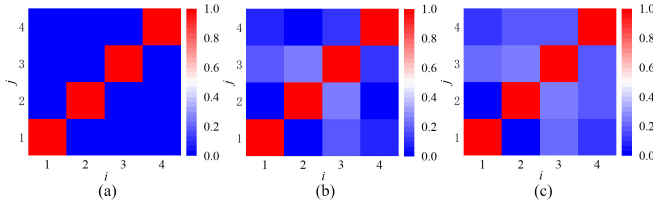
**FIGURE 7.** Modal far-field orthogonality for (a) the butterfly-shaped structure, (b) the butterfly-shaped structure with $R_s=30\,\mathrm{Ohm}$ and (c) the butterfly-shaped structure with the resistances $R_a=20\,\mathrm{Ohm}$ ($R_s=30\,\mathrm{Ohm}$) at 10 GHz.



**FIGURE 9.** CM analysis for the butterfly-shaped structure loaded different $R_a$ ($R_s=30\,\mathrm{Ohm}$) (a) MSs and (b) MWCs.



**FIGURE 8.** Evaluation for the absorption performance of the butterfly-shaped structure with $R_s=30\,\mathrm{Ohm}$.



**FIGURE 10.** Evaluation for the absorption performance of the structure with $R_a=20\,\mathrm{Ohm}$ ($R_s=30\,\mathrm{Ohm}$).

narrow-band absorption is achieved at the resonant frequency of mode 1. Moreover, it is found that the evaluated results converge when the mode order is up to 4 as the $\alpha_n$ of other high-order modes are very small.

To improve the absorption broadband, there are two options to deal with mode 4.

(i) The first method, similar to mode 1, is to convert the scattered power of mode 4 into thermal power by loading impedance. According to the current distribution of mode 4, as shown in Fig. 6(c), the resistances $R_a$ are loaded on the microstrip line where the $\mathbf{J}_4$ is concentrated. The far-field nonorthogonality of the two significant modes (mode 1 and mode 4) can also be neglected, as shown in Fig. 7(c). Fig. 9 shows the MSs and MWCs of the first four modes and the reflection coefficient $S_{11}$ evaluated with the first four CMs is given in Fig. 10. The result shows that dual-band absorption has been achieved at the resonant frequencies of mode 1 and mode 4. Optimizing the impedance $R_s$ and $R_a$ can effectively improve the absorption bandwidth. However, it will not be further discussed here considering that in practice loading components on microstrip line is not easy and the complexity introduced by the modal far-field orthogonality discussion.

(ii) The second method is to suppress the MS of mode 4 in the band of interest by increasing the absolute value of $\lambda_4$. Fig. 11(a) shows the value of $\lambda_4$ is less than 0 near the resonant frequency, which exhibits capacitive features of mode 4 in the band of interest. By inserting a capacitance $C_v = 0.1\mathrm{pF}$ at the place where the horizontal component of
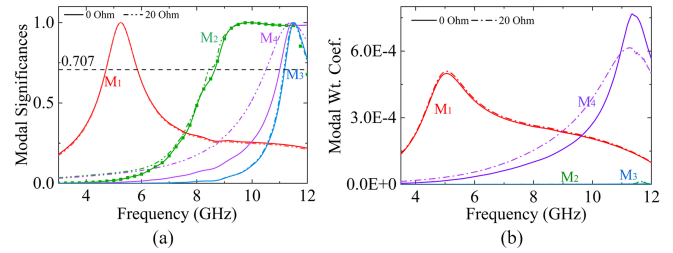
$\mathbf{J}_4$ is concentrated, the results indicate that the absolute value of $\lambda_4$ can be effectively increased while the other modes are almost unaffected. Thus, as shown in Fig. 11(b) and (c), the significance of mode 4 is suppressed in the band of interest. In addition, the MWCs of the structure are illustrated in Fig. 11(d). It can be seen clearly that mode 1 has the largest MWC in the band of interest and shifts to higher frequencies as $R_s$ increases, while the other modes have very small MWCs. The surface current $\mathbf{J}$ of the structure with $C_v = 0.1\mathrm{pF}$ is mainly dominated by $\mathbf{J}_1$. The reflection coefficients $S_{11}$ evaluated with the first four CMs are given in Fig. 12. The results show that the absorption bandwidth of the butterfly-type structure loaded with PIN diode can be enhanced by impedance modulation.

### D. Full-wave Validation and Finalization.

The full-wave simulations are carried out to obtain the reflection coefficients at normal incidence using CST Microwave Studio software. The reflection coefficients of the structure shown in Fig. 8 and Fig. 10 are given, respectively, and they are in good agreement with the evaluated ones, validating the CM analysis. The slight difference in amplitude and resonance frequency could be attributed to the approximation adopted in the CM analysis.

The full-wave simulations are also performed to finalized the broadband optimization results. It should be noted that $w = 1.1$ mm, $l = 2.8$ mm are used here to meet the size requirements of surface-mounted (SMT) for the components. According to the results of parameter study shown in Fig.
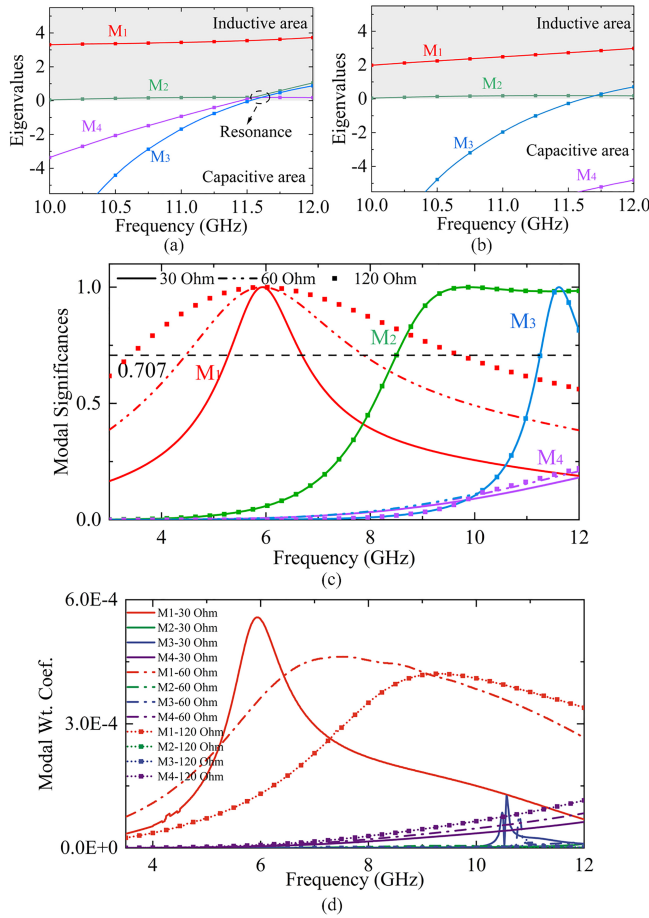
**FIGURE 11. CM analysis for the butterfly-shaped structure with $C_v = 0.1\text{pF}$. (a) Eigenvalues without capacitance, (b) eigenvalues with capacitance, (c) MSs and (d) MWCs with different $R_s$.**
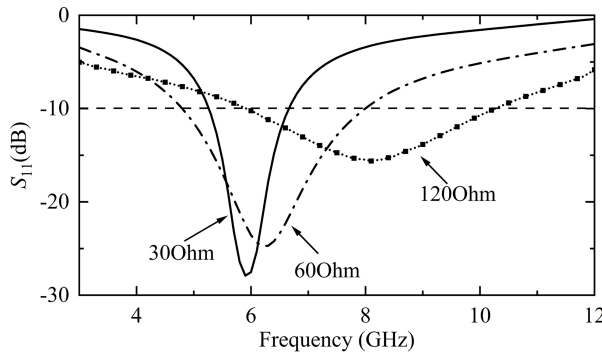


**FIGURE 12. Evaluation for the absorption performance of the structure with different $R_s$.**

5, a change in $l$ does not affect mode 1 operating state of the butterfly-shaped structure, whereas a change in $w$ does. Hence, the structural impact of the change in $w$ is reduced by optimizing parameters $b = 2.2$ mm, $g = 0.9$ mm and $C_v = 0.5$ pF. Fig. 13 shows the reflection coefficients of the final element with different $R_s$. When the PIN diode is switched OFF, near perfect reflection is obtained over a broadband from 3 to 12 GHz. As shown in Fig. 13(a),
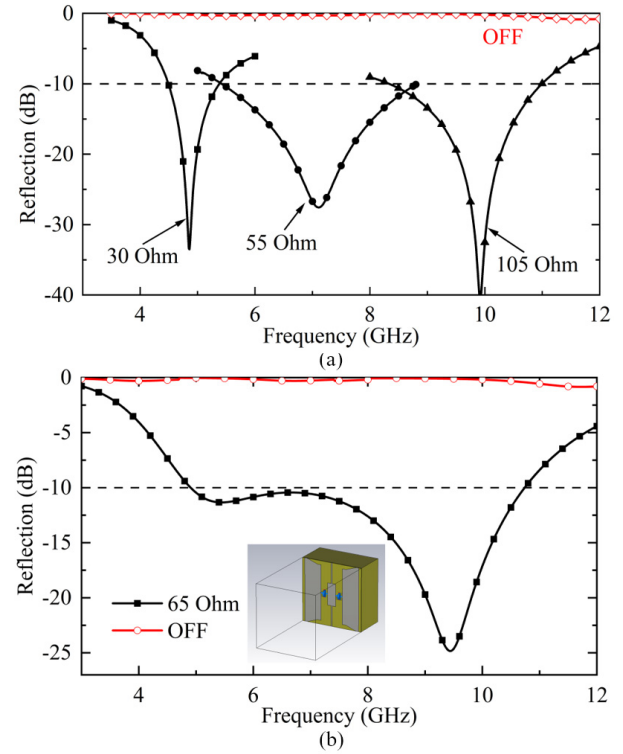


**FIGURE 13. Reflection coefficient of the final element under normal illumination. (a) Broadband absorption based on multistate modulation and (b) broadband absorption with optimizing $R_s = 65$ Ohm.**

when the $R_s$ of PIN diode increases from 0 to 30 Ohm, 55 Ohm and 105 Ohm, high absorption are obtained at 4.9 GHz, 7.2 GHz and 10 GHz, respectively. Furthermore, broadband absorption with reflection coefficient less than -10 dB from 4.8 GHz to 10.7 GHz can be achieved when optimizing the $R_s = 65$ Ohm as shown in Fig. 13(b). Although the $R_s$ corresponding to the resonant frequencies are slightly different due to the optimization of finalized, it demonstrates the CM design of the element for broadband absorption with multistate switching. The CM-based design procedures are illustrated in Fig. 14.

The power flow distribution of the final element is also investigated to gain insight into the absorption properties. With all three frequencies, as shown in Fig. 15, it is clear that the input power is mainly concentrated around the PIN diode and inescapably is converted into thermal power, which means that the input power is absorbed. This is consistent with the CM analysis of the low scattering mechanism.

### E. Further Improvement for Conformal Metasurface

In practical applications, flexible metasurface are preferred for objects with free-form surface. To this end, influenced by demand for flexible printed circuit (FPC) processes, the top metallic layer is printed on a 0.1 mm thick polyimide (PI) with a relative dielectric constant of 3.5 and a loss tangent angle of 0.0027. A substrate of flexible polyvinyl chloride (PVC) with a relative dielectric constant of 3, loss tangent of 0.014, and thickness of 3.8 mm is chosen. The dimensions
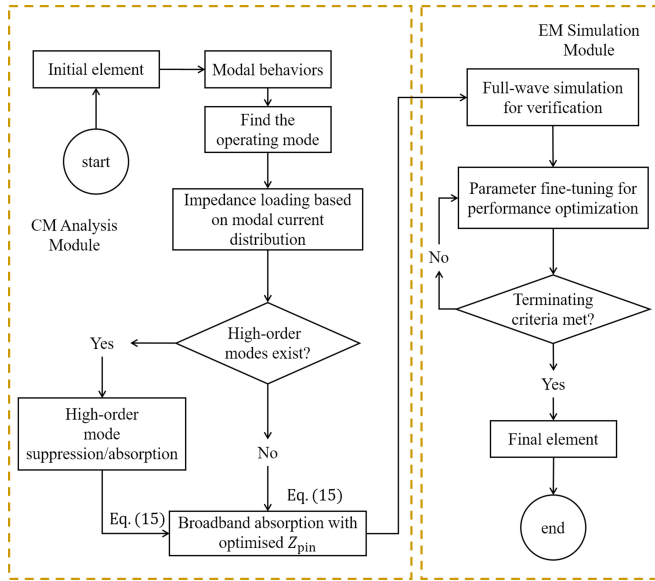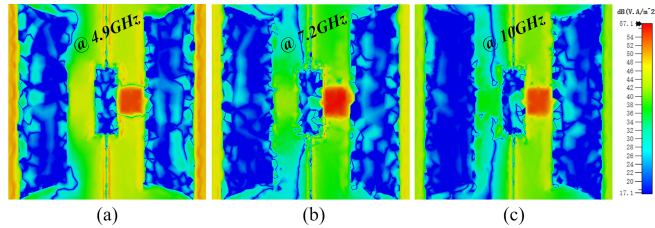
FIGURE 14. Flowchart of the design procedure.



FIGURE 15. Power flow distributions of the final element at (a) 4.9 GHz, (b) 7.2 GHz, and (c) 10 GHz.



FIGURE 16. Simulated absorption rate of the flexible element with different $R_s$ under oblique incident.



FIGURE 17. Simulated SCS results for different states of the half-cylinder model under normal incidence.

of the butterfly-shaped structure remain unchanged. Firstly, the absorption performance of the flexible element at oblique incidence angles is verified. As shown in Fig. 16, the element exhibits a stable absorption in the incidence range of 45 at 4.9 GHz, but as the increase of incident angle, the resonant frequency shifts to higher frequencies. While the AR is reduced to about 0.8 when the incidence angle is 45 at 7.2 and 10 GHz. This is due to the difference in propagation phase caused by oblique incidence on the metasurface, which has a more significant effect at higher frequency [46]. Then, a half-cylinder model with 0.2 m height and 0.5 m diameter containing $96{\times}24$ flexible elements is numerically simulated. The bend-shape function of CST Microwave Studio is used to bend the element structure into an arc to form the cylinder. Considering the huge time requirements for simulations of the whole half-cylinder model, only the absorption performance of low frequency is verified numerically. The simulated SCSs for the conformal metasurface with the number of OFF-state elements reduced by column are shown in Fig. 17. It is observed that the SCS of the half-cylinder conformal metasurface can be dynamically varied from -27 ($R_s$= 30 Ohm) to -5 dB (OFF state) around 5 GHz, where different states represent different numbers of absorbing elements in the array. This is consistent with the reflection
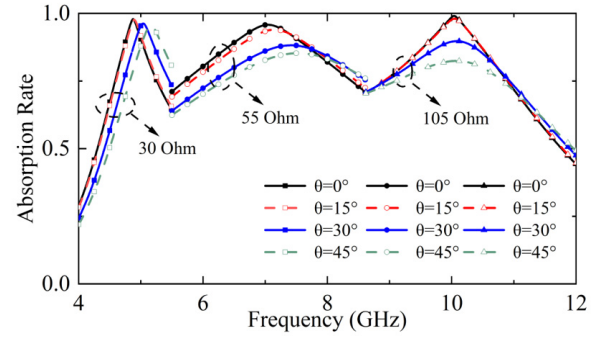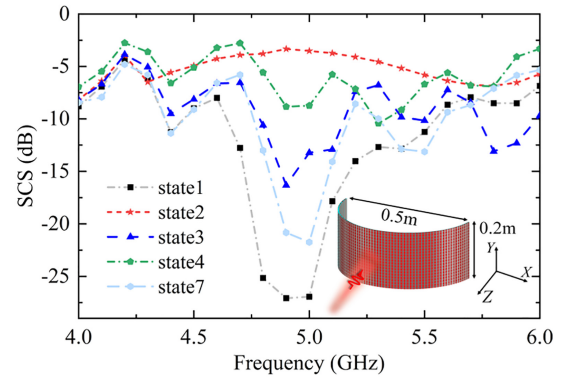
coefficient of the designed element as its good absorption performance at oblique incidences.

## IV. EXPERIMENTS AND DISCUSSIONS
In order to experimentally verify the proposed broadband tunable MMA, a flexible prototype consisting $24 \times 24$ elements is fabricated by FPC, 1152 capacitors and PIN diodes are loaded onto the elements by SMT as shown in Fig. 18(a), (b). The dimension of the entire fabricated prototype are $202$ mm $\times 202$ mm, which are determined by the FPC technology (less than 250 mm) so that four prototypes form a half-cylindrical model. The FPGA is employed to program the amplitude of output currents, and each input/output (I/O) port can independently output currents from 0 to 250 mA with a minimum step of 0.06 mA.

The absorption performances of the fabricated prototypes are tested in an anechoic chamber, as shown in Fig. 18(c), in which a pair of broadband linearly polarized horn antennas are selected as the transmitter and receiver. The vector network analyzer of Agilent N5227A with two ports is connected to the antennas. The transmitting and receiving antennas are placed 3 m and 4 m away from the absorber respectively to ensure the incidence of horizontally polarized plane wave. To exclude interference from the surrounding environment and coupling between the two antennas, the time domain gating function of the vector network analyzer is used in the test. During the measurement, equal-sized
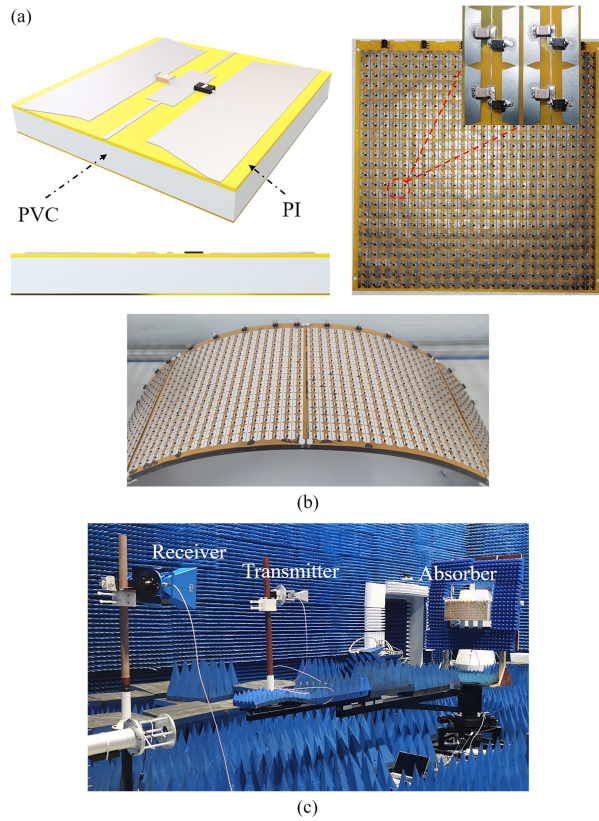
FIGURE 18. **(a) Prototype of the MMA, (b) half-cylindrical model, and (c) measurement setup.**

metal is covered on the foams for calibration, the SCS reduction of the metasurface can be calculated as

$$\mathrm{SCS_r\,(dB)} = 10\log\left(\frac{\mathrm{SCS_{meta}}}{\mathrm{SCS_{gnd}}}\right) = 10\log\left(\frac{\left|\mathrm{E^s_{meta}}\right|^2}{\left|\mathrm{E^s_{gnd}}\right|^2}\right) \tag{13}$$

It can be used to represent the absorption performance of the MMA when all the elements of the metasurface are in the same state.

TABLE 1. **Resistance of PIN Diodes in the Test**

| Output Current (mA) | Bias Current (mA) | Resistance (Ohm) Sim./Mea. |
|---|---|---|
| 40.6 | 1.7 | 30/23 |
| 22.5 | 0.94 | 55/36 |
| 29.4 | 1.23 | 65/42 |
| 8 | 0.33 | 105/102 |

First, fabricated prototypes located on the flat foam are tested to verify the absorption performance. By gradually increasing the amplitude of output currents from 0 to 75 mA, the results in Fig. 19(a) show that three strong absorption states for planar metasurface are realized at 5.5 GHz, 7.3 GHz and 10.4 GHz, corresponding to 40.6 mA, 29.4 mA, and 8.0 mA respectively. Next, as shown in Fig. 19(b), the SCS
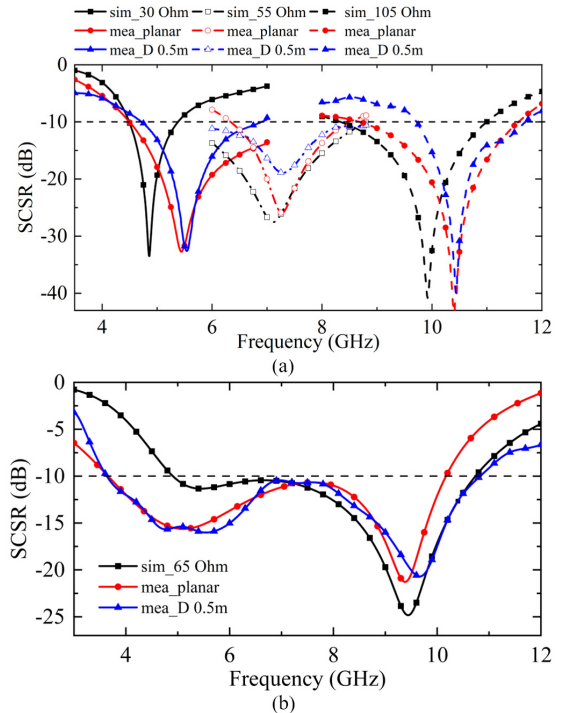


FIGURE 19. **Measured SCS reduction (SCSR) of the proposed MMA located on planar and conformal foams. (a) Broadband absorption based on multistate modulation, (b) broadband absorption from 3.6 GHz to 10.2 GHz. The simulated results are presented for comparison.**

reduction bandwidth below -10 dB is realized from 3.6 GHz to 10.2 GHz when the output current is carefully adjusted to 22.5 mA. As a result, a total broadband absorption from 3.6 GHz to 11.6 GHz (105%) can be achieved by using multistate switching. According to the NXP diode datasheet, Table I lists the simulated and actual measured equivalent resistances $R_s$ for comparison, where the measured impedance is obtained by checking chart. It can be seen that the above measured results are consistent with the simulated ones in principle, slight discrepancies may be due to the following reasons.

1) Fabrication and testing tolerance.

2) The actual operating frequencies of the MMA higher than the typical test frequency shown in the datasheet.

3) The effect of diffusion capacitance from PIN diodes under forward bias.

Then, the fabricated prototypes located on a cylindrical foam with 0.5 m diameter are tested. The results show similar absorption performances of the proposed MMA in both planar and cylindrical cases, verifying the absorption performance of the element under oblique incidence. In addition, to extend the application range of the MMA, Fig. 20(b), and (c) show the SCS reduction curves by changing the I/O port output current of the FPGA from 0 to 75 mA, which can be precisely switched in the range of -30 dB with an accuracy better than 1.5 dB. With the measured SCS dataset, the corresponding output current states can be encoded according to the required SCS by pre-optimizations [8]. For example, as shown in Fig. 20, the SCS of the MMA
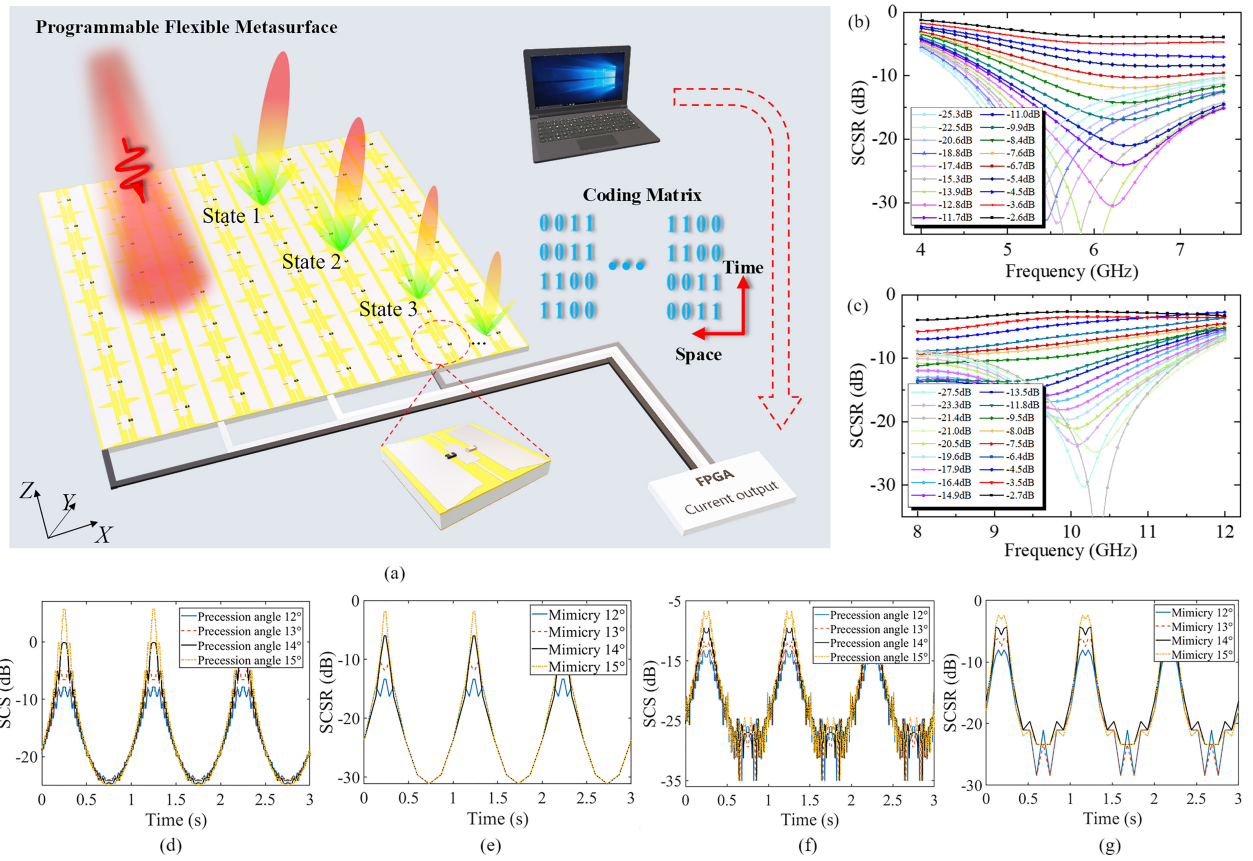
**FIGURE 20.** (a) Schematic of the proposed MMA. The MMA consists of a PIN diode-loaded flexible metasurface and peripheral modulator control circuits. The used modulator control circuits incorporate a high-precision current output module and field programmable gate array (FPGA), which can output multi-path currents from 0 to 240 mA with 0.06 mA accuracy. By applying elaborately designed space-time modulated output currents to the metasurface, high accurate dynamic modulation sequence of the scattering states can be achieved. Dynamic modulation measurements of SCS reduction by FPGA at (b) 5 GHz and (c) 10 GHz. The application in mimicking the time-varying SCS of a typical cone target of (d) SCS with different precession angles by the fast integral solver and (e) mimetic results at 5 GHz; (f) SCS with different precession angles by the fast integral solver and (g) mimetic results at 10 GHz.

**TABLE 2.** Performance Composition of Previously Reported MMAs

| Ref. | BW Frequency (GHz) | Reconfigurable | Flexibility | Regulation Accuracy (dB) | Oblique Incident (°) | Relative Thickness ($\lambda_c$[1]) | Methodology |
|---|---|---|---|---|---|---|---|
| [14] | 2.2-8.9 (126%) | NO | NO | N/A | 30 | 0.27 | ECM |
| [16] | 1-4.5 (127%) | NO | YES | N/A | N/A | 0.25 | TCM |
| [29] | 0.4-2.5 (145%) | YES | NO | N/A | 45 | 0.13 | ECM |
| [30] | 2-11.3 (140%) | YES | NO | N/A | N/A | 0.20 | ECM |
| [31] | 3.9-11.0 (95%) | YES | NO | 2.5 dB | 30 | 0.19 | ECM |
| [32] | 8.5-18.2 (130%) | YES | NO | 4 dB | 30 | 0.11 | ECM |
| **This work** | **3.6-11.6 (105%)** | **YES** | **YES** | **1.5 dB** | **45** | **0.10** | **TCM** |

[1] $\lambda_c$: wavelength of the center frequency.

is coded in real-time by FPGA to achieve the mimicry of the micro-motion features of the cone-shaped object (its height and diameter are 1.8 m and 0.5 m, respectively). Where the SCS results of the cone-shaped object in the C/X dual-band are obtained by fast integral solver [47] with the angle interval of 0.1° and frequency interval of 2 MHz. Then, using the SCS results, the scattered fields with different precession angles in the frequencies of 5 GHz and 10 GHz are calculated under the conditions of 65° scattering

aspect angle and 1 s precession period. Very good mimicry performances are achieved as in Fig. 20(d)-(g).

Table II lists detailed comparisons between the proposed MMA and previously reported ones in the literature. As can be seen, the proposed MMA has reconfigurable function and a lower profile compared to [14], [17]. The absorbers shown in [29]-[32] feature a good reconfigurable absorption bandwidth, but the rigid nature of the structure limits some of their application scenarios. As a result, the proposed MMA has exhibited the benefits of flexible implementation, lower

profile, and high-precision modulation of real-time SCS. Compare with other efforts based on traditional methods, CM design for the MMA can provide visual modal behaviors with clear underlying EM physics to guide the design process of element efficiently.

## V. CONCLUSION

A CM-based design methodology for the tunable MMAs with using commercially available substrates is developed through revealing the theoretical intrinsic connection between modal behaviors and absorption properties. With the aid of the guideline, a broadband tunable MMA has been designed, fabricated, and measured. The TCM has been introduced to guide the design, analysis and optimization of low scattering features of the butterfly-shaped element. Flexible implementation is given to the structure to fit practical applications with free-form surfaces. Both planar and conformal MMAs are experimentally verified. Broadband SCS reduction in the range of 3.6-11.6 GHz (105%) with multistate modulation are achieved by encoding the FPGA output currents, which clearly demonstrates the effectiveness of the developed CM-based design methodology.

## REFERENCES

[1] K. N. Rozanov, "Ultimate thickness to bandwidth ratio of radar absorbers," *IEEE Trans. Antennas Propag.*, vol. 48, no. 8, pp. 1230-1234, Aug 2000.

[2] M. Amano and Y. Kotsuka, "A method of effective use of ferrite for microwave absorber," *IEEE Trans. Microw. Theory Techn.*, vol. 51, no. 1, pp. 238-245, Jan. 2003.

[3] C. P. Neo and V. K. Varadan, "Optimization of carbon fiber composite for microwave absorber," *IEEE Trans. Electromagn. Compat.*, vol. 46, no. 1, pp. 102-106, Feb. 2004.

[4] B. Chambers, "Optimum design of a Salisbury screen radar absorber," *Electron. Lett.*, vol. 30, no. 16, pp. 1353C1354, Aug. 1994.

[5] L. J. Du Toit, and J. H. Cloete, "Electric screen Jauman absorber design algorithms," *IEEE Trans. Microw. Theory Techn.*, vol. 44, no. 12, pp. 2238-2245, Dec. 1996.

[6] C. M. Watts, X. L. Liu, and W. J. Padilla, "Metamaterial electromagnetic wave absorbers," *Adv. Mater.*, vol. 24, no. 23, pp. 98-120, May 2012.

[7] F. Costa and A. Monorchio, "A frequency selective radome with wideband absorbing properties," *IEEE Trans. Antennas Propag.*, vol. 60, no. 6, pp. 2740-2747, June 2012.

[8] S. H. Zhou, X. Y. Fang, M. Li, Y. F. Yu, and R. S. Chen, "S/X dual-band real-time modulated frequency selective surface based absorber," *Acta Phys. Sin.*, vol. 69, Art. no. 204101, 2020.

[9] T. -X. Feng, and L. Zhu, "Ultra-wideband 3-D microwave absorbers with composite slotlines and microstrip lines: synthetic design and implementation," *IEEE Open J. Antennas Propag.*, vol. 4, pp. 303-311, 2023.

[10] C. L. Holloway, E. F. Kuester, J. A. Gordon, J. Hara, J. Booth, and D. R. Smith, "An overview of the theory and applications of metasurfaces: the two-dimensional equivalents of metamaterials," *IEEE Antennas Propag. Mag.*, vol. 54, no. 2, pp. 10C35, July 2012.

[11] C. Fu, L. Han, C. Liu, Z. Sun, and X. Lu, "Dual-band polarization conversion metasurface for RCS reduction," *IEEE Trans. Antennas Propag.*, vol. 69, no. 5, pp. 3044-3049, May 2021.

[12] L. Wang, S. Liu, X. Kong, H. Zhang, Q. Yu, Y. Wen, and D. Wango, "A multifunctional frequency-selective polarization converter for broadband backward-scattering reduction," *IEEE Trans. Antennas Propag.*, vol. 69, no. 5, pp. 2833-2841, May 2021.

[13] N. I. Landy, S. Sajuyigbe, J. Mock, D. R. Smith, and W. J. Padilla, "Perfect metamaterial absorber," *Phys. Rev. Lett.*, vol. 100, Art. no. 207402, May 2008.

[14] Y. Shang, Z. Shen, and S. Xiao, "On the design of single-layer circuit analog absorber using double-square-loop array," *IEEE Trans. Antennas Propag.*, vol. 61, no. 12, pp. 6022-6029, Dec. 2013.

[15] B. Zhang, C. Jin, and Z. Shen, "Low-profile broadband absorber based on multimode resistor-embedded metallic strips," *IEEE Trans. Microw. Theory Techn.*, vol. 68, no. 3, pp. 835-843, March 2020.

[16] D. Zha, J. Dong, Z. Cao, Y. Zhang, F. He, R. Li, Y. He, L. Miao, S. Bie, and J. Jiang, "A multimode, broadband and all-inkjet-printed absorber using characteristic mode analysis," *Opt. Express*, vol. 28, no.6, pp. 8609C8618, 2020.

[17] Y. Zhuang, G. Wang, J. Liang, T. Cai, W. Guo, and Q. Zhang, "Flexible and polarization-controllable diffusion metasurface with optical transparency," *J. Phys. D: Appl. Phys.*, vol. 50, Art. no. 465102, Oct. 2017.

[18] N. Karl, P. P. Vabishchevich, M. R. Shcherbakov, S. Liu, M. B. Sinclair, G. Shvets, and I. Brener, "Frequency conversion in a time-variant dielectric metasurface," *Nano Let.*, vol. 20, no. 10, pp. 7052-7058, Oct. 2020.

[19] S. Yin, D. Xiao, J. Liu, K. Li, H. He, S. Jiang, D. Luo, X. W. Sun, W. Ji, and Y. J. Liu, "Reconfigurable chiral metasurface absorbers based on liquid crystals," *IEEE Photon. J.*, vol. 10, no. 6, pp. 1-9, Dec. 2018.

[20] M. Sun, X. Xu, X. W. Sun, X. Liang, V. Valuckas, Y. Zheng, and A. I. Kuznetsov, "Efficient visible light modulation based on electrically tunable all dielectric metasurfaces embedded in thin-layer nematic liquid crystals," *Sci. Rep.*, vol. 9, Art. no. 8673, 2019.

[21] A. Forouzmand and A. B. Yakovlev, "Electromagnetic cloaking of a finite conducting wedge with a nanostructured graphene metasurface," *IEEE Trans. Antennas Propag.*, vol. 63, no. 5, pp. 2191-2202, Feb. 2015.

[22] H. Chen, W. -B. Lu, Z. -G. Liu, J. Zhang, A. -Q. Zhang, and B. Wu, "Experimental demonstration of microwave absorber using large-area multilayer graphene-based frequency selective surface," *IEEE Trans. Microw. Theory Techn.*, vol. 66, no. 8, pp. 3807-3816, Aug. 2018.

[23] J. Han and R. S. Chen, "Tunable broadband terahertz absorber based on a single-layer graphene metasurface," *Opt. Express*, vol. 28, no. 20, pp. 30289-30298, 2020.

[24] S. Ghosh and S. Lim, "Fluidically switchable metasurface for wide spectrum absorption," *Sci. Rep.*, vol. 8, Art. no. 10169, 2018.

[25] T. Debogovic and J. Perruisseau-Carrier, "Low loss MEMS-reconfigurable 1-bit reflectarray cell with dual-linear polarization," *IEEE Trans. Antennas Propag.*, vol. 62, no. 10, pp. 5055C5060, Oct. 2014.

[26] X. Gao, W. L. Yang, H. F. Ma, Q. Cheng, X. H. Yu, and T. J. Cui, "A reconfigurable broadband polarization converter based on an active metasurface," *IEEE Trans. Antennas Propag.*, vol. 66, no. 11, pp. 6086C6095, Nov. 2018.

[27] F. Costa, A. Monorchio, and G. P. Vastante, "Tunable high-impedance surface with a reduced number of varactors," *IEEE Antennas Wireless Propag. Lett.*, vol. 10, pp. 11C13, 2011.

[28] C. Huang, C. Zhang, J. Yang, B. Sun, B. Zhao, and X. Luo, "Reconfigurable metasurface for multifunctional control of electromagnetic wave," *Adv. Opt. Mater.*, vol. 5, Art. no. 1700485, Sep. 2017.

[29] Y. Zhang, Z. Cao, Z. Huang, L. Miao, S. Bie, and J. Jiang, "Ultrabroadband double-sided and dual-tuned active absorber for UHF band," *IEEE Trans. Antennas Propag.*, vol. 69, no. 2, pp. 1204-1208, Feb. 2021.

[30] J. Li, J. Jiang, Y. He, W. Xu, M. Chen, L. Miao, and S. Bie, "Design of a tunable low-frequency and broadband radar absorber based on active frequency selective surface," *IEEE Antennas Wireless Propag. Lett.*, vol. 15, pp. 774-777, 2016.

[31] S. Guo, Y. Zhao, Q. Cao, Z. Mao, J. Dong, S. Bie, L. Miao, and J. Jiang, "Multistate active control RCS signature for the continuous adjustment absorber/reflector transformation applications," *Opt. Express*, vol. 29, no. 15, pp. 24151-24160, 2021.

[32] B. Zhao, C. Huang, J. Yang, J. Song, C. Guan, and X. Luo, "Broadband polarization-insensitive tunable absorber using active frequency selective surface," *IEEE Antennas Wireless Propag. Lett.*, vol. 19, no. 6, pp. 982-986, June 2020.

[33] X. Y. Fang, M. Li, D. Z. Ding, F. Billotti, and R. S. Chen, "Design of in-phase and quadrature two paths space-time-modulated metasurfaces," *IEEE Trans. Antennas Propag.*, doi: 10.1109/TAP.2022.3145480, 2022.

This article has been accepted for publication in IEEE Open Journal of Antennas and Propagation. This is the author's version which has not been fully edited and content may change prior to final publication. Citation information: DOI 10.1109/OJAP.2023.3336610

**IEEE Open Journal of**
**Antennas and Propagation**

[34] R. Harrington and J. Mautz, "Theory of characteristic modes for conducting bodies," *IEEE Trans. Antennas Propag.*, vol. 19, no. 5, pp. 622C628, Sep. 1971.

[35] Y. Chen and C.-F. Wang, *Characteristic Modes: Theory and Applications in Antenna Engineering*, John Wiley & Sons, Inc., 2015.

[36] C. Zhao, and C. F. Wang, "Characteristic mode design of wide band circularly polarized patch antenna consisting of H-shaped unit cells," *IEEE Access*, vol. 6, pp. 25292 - 25299, April 2018.

[37] D. Zha, Z. Cao, R. Li, F. He, K. Si, J. Dong, L. Miao, S. Bie, and J. Jiang, "A physical insight into reconfigurable frequency selective surface using characteristic mode analysis," *IEEE Antennas Wireless Propag. Lett.*, vol. 20, no. 10, pp. 1863-1867, Oct. 2021.

[38] T. Li, J. Sun, H. Meng, Y. Shen, S. Hu, W. Dou, and Z. N. Chen, "Characteristic mode inspired dual-polarized double-layer metasurface lens," *IEEE Trans. Antennas Propag.*, vol. 69, no. 6, pp. 3144-3154, June 2021.

[39] Q. Guo, J. Su, Z. Li, J. Song, and Y. Guan, "Miniaturized-element frequency-selective rasorber design using characteristic modes analysis," *IEEE Trans. Antennas Propag.*, vol. 68, no. 9, pp. 6683-6694, Sept. 2020.

[40] F. Ling and J.-M. Jin, "Scattering and radiation analysis of microstrip antennas using discrete complex image method and reciprocity theorem," *Microw. Opt. Techn. Lett.*, Vol. 16, no. 4, Nov. 1997.

[41] C.-F. Wang, F. Ling, and J.-M. Jin, "A fast full-wave analysis of scattering and radiation from large finite arrays of microstrip antennas," *IEEE Trans. Antennas Propag.*, vol. 46, no. 10, Oct. 1998.

[42] P. Ylä-Oijala, H. Wallén, S. Järvenpää, "Theory of characteristic modes for lossy structures: Formulation and interpretation of eigenvalues," *Int. J. Numer. Model.*, vol. 33, Art. no. e2627, May 2020.

[43] D. Jiao and J.-M. Jin, "Fast frequency-sweep analysis of RF coils for MRI," *IEEE Trans. Biomed. Eng.*, vol. 46, no. 11, pp. 1387-1390, Nov. 1999.

[44] NXP, "BAP series: low inductance, low capacitance, SMD plastic package PIN diodes," March 2014. [Online]. Available https://www.nxp.com/data-sheet/BAP70-03.pdf.

[45] P. Sumithra and D. Kannadassan, "Design and Modeling of Wideband Planar Antennas Using Characteristics Modes," *IEEE Trans. Antennas Propag.*, vol. 69, no. 12, pp. 8257-8270, Dec. 2021.

[46] F. Li, L. Zhang, P. Zhou, H. Chen, R. Zhao, Y. Zhou, D. Liang, H. Lu, and L. Deng, "Dual-band reflective polarization converter based on slotted wire resonators," *Appl. Phys. B*, vol. 124, Art. no. 28, Jan. 2018.

[47] M. Li, Y. Hu, R. S. Chen, and G. Vecchi, "Electromagnetic modeling of moving mixed conductive and dielectric BoRs with an effective domain decomposition method," *IEEE Trans. Antennas Propag.*, vol. 68, no. 12, pp. 7978-7985, Dec. 2020.

Communication Engineering, Nanjing University of Science and Technology, where he has been an Assistant Professor, Associate Professor, and Professor since 2020. In 2017, he was a Visiting Scholar with Pennsylvania State University, State College, PA, USA. His research interests include fast solver algorithms, computational electromagnetic solvers for circuits, signal integrity analysis, and multiscale simulations.

Dr. Li was the recipient of the National Science Fund for Excellent Young Scholars in 2022, Young Scientist Award at the ACES China Conference in 2019, Doctoral Dissertation Award of Jiangsu Province in 2016, and seven student paper/contest awards at the international conferences with the students. He is an Associate Editor for *IEEE Antennas and Propagation Magazine*, *IEEE Open Journal of Antennas and Propagation* (OJAP), and *IEEE Access*, and the Guest Editor of OJAP.

**Dazhi Ding** (Senior Member, IEEE) received the B.Sc. and Ph.D. degrees in electromagnetic field and microwave technique from the Nanjing University of Science and Technology (NJUST), Nanjing, China, in 2002 and 2007, respectively. In 2005, he was with the Center of wireless Communication, City University of Hong Kong, Hong Kong, as a Research Assistant. He joined the Department of Electrical Engineering, NJUST, where he became a Lecturer in 2007. In 2014, he was promoted to Full Professor in NJUST, where he was appointed as the Head of the Department of Communication Engineering, in September 2014. He is the author or coauthor of over 30 technical articles. He has authored or coauthored more than 80 articles. His current research interests include computational electromagnetics and electromagnetic scattering and radiation.

Dr. Ding was a recipient of the National Excellent Youth Fund by the National Science Foundation of China (NSFC) in 2020.

**Xia Ai** was born in Yulin, China, in 1986. He received the Ph.D. degree in electromagnetics and microwave technology from Xidian University, Xi'an, China, in 2013. He is currently a Senior Engineer with the National Key Laboratory of Science and Technology on Test Physics and Numerical Mathematics. His research interests include computational electromagnetics, radar target recognition, and electromagnetic scattering characteristic of complex medium.

**Zihao Ning** was born in Fuyang, China, in 1998. He received the B.S. degree in electronic information engineering from Nanjing University of Science and Technology (NJUST), Nanjing, China, in 2020. He is currently pursuing the Ph.D. degree in electronic science and technology with NJUST, Nanjing, China. His research interests include theory of characteristic modes, computational electromagnetics and metasurface.

**Jiaqi Liu** was born in Yueyang, China, in 1963. He received the Ph.D. degree in circuit and systems from Beihang University, Beijing, China, in 2007. He currently serves as the Vice Director and leading Research Fellow with the National Key Laboratory of Science and Technology on Test Physics and Numerical Mathematics. His research area is signal processing and target recognition.

**Mengmeng Li** (Senior Member, IEEE) received the B.S. degree (Hons.) in physics from Huaiyin Normal College, Huai'an, China, in 2007, and the Ph.D. degree in electromagnetic field and microwave technology from the Nanjing University of Science and Technology, Nanjing, China, in 2014. From 2012 to 2014, he was a Visiting Student with the Electronics Department, Politecnico di Torino, Turin, Italy, and also with the Antenna and EMC Laboratory, Istituto Superiore Mario Boella, Turin, where he carried out fast solver for multiscale simulations. Since 2014, he has been with the Department of

**Chao-Fu Wang** (Senior Member, IEEE) received the B.Sc. degree in mathematics from Henan Normal University, Xinxiang, China, in 1985, the M.Sc. degree in applied mathematics from Hunan University, Changsha, Hunan Province, China, in 1989, and the Ph.D. degree in electrical engineering from the University of Electronic Science and Technology of China, Chengdu, China, in 1995.

From 1987 to 1996, he was a Lecturer and then an Associate Professor with the Nanjing University of Science and Technology, Nanjing, China.

From 1996 to 1999, he was a Postdoctoral Research Fellow with the Center for Computational Electromagnetics, University of Illinois at Urbana-Champaign, Urbana, IL, USA. He came to Singapore in 1999 to join the National University of Singapore and became a Principal Research Scientist in 2011. He has coauthored *Characteristic Modes: Theory and Applications in Antenna Engineering* (Hoboken, NJ: Wiley, 2015). He has published more than 280 journal and conference papers and filed six patents published under the Patent Cooperation Treaty (PCT) administered by the World Intellectual Property Organization (WIPO) in the area of computational electromagnetics.

Dr. Wang was a co-recipient of the 2009 Best *Applied Computational Electromagnetics Society (ACES) Journal* Paper Award. He served as the Chairperson for the IEEE Singapore Microwave Theory and Techniques/Antennas and Propagation (MTT/AP) Chapter in 2013. He has been actively involved in organizing many conferences, including the General Chair of 2020 IEEE International Conference on Computational Electromagnetics (ICCEM 2020). As a regular reviewer of many international journals, he was an Associate Editor of the *IEEE Transactions on Microwave Theory and Techniques* from 2020 to 2022, and he is currently an Associate Editor of *IEEE Journal on Multiscale and Multiphysics Computational Techniques*, *International Journal of Numerical Modelling: Electronic Networks*, *Devices and Fields*, and *Electronics Letters*. As a Guest Editor of the *International Journal of Numerical Modelling: Electronic Networks*, *Devices and Fields*, he has successfully edited a special issue (volume 33, issue 2, March/April 2020) on advanced solution methods for modeling complex electromagnetic problems.